Science of Sintering, **54** (2022) 265-285

https://doi.org/10.2298/SOS2203265D

UDK: 677.017.5; 692.533.1; 546.562

Exploring the Optical and Electrical Characteristics of $CuO/CuCo_2O_4$ Composites

Nasrallah. M. Deraz[1*)], Hisham A. Saleh[2], Amal M. Abdel-karim[1]

[1]Physical Chemistry Department, National Research Centre, 33 El Bohouth St. (El-Tahrir St. former), Dokki, Giza, Egypt-P.O.12622.

[2]Electron Microscope and Thin Films Department, National Research Centre, 33 El Bohouth St. (El-Tahrir St. former) Dokki, Giza, Egypt- P.O.12622.

Abstract:

Series of $CuO/CuCo_2O_4$ composites were prepared by using the combustion method followed by heating at 750^{o}C with different molar ratios of Cu/Co. Characterization of different composites is systematically investigated with various analytical techniques. X-ray diffraction patterns and Fourier-transform infrared spectroscopy indicate the growth of well crystalline $CuCo_2O_4$ nanoparticles with a cubic spinel structure. Images of transmission electron microscope and scanning electron microscope show a uniform particle distribution. From UV-visible spectra, the calculated optical band gaps of various solids were ranged between 1.2 and 1.8 eV. Electrical properties were measured at temperature ranged from 303 to 463 K in a frequency range from 102 to 106 Hz. The AC conductivity satisfied the Jonscher equation, especially at high frequency. The obtained data of conductivity and dielectric constant indicated that the prepared samples behave as semiconductor materials. Finally, it can be concluded that the $CuO/CuCo_2O_4$ composite showed attractive multi-functional features for electrical applications.

Keywords: *$CuO/CuCo_2O_4$ composite; Optical properties; Conductivity; Dielectric constant; Semiconductor.*

1. Introduction

Recently, nanostructure materials have unprecedented properties ultimately causing a number of applications within the technological area for research, and advancement activity. These materials have distinctive properties such as low optical energy band gap and high electrical conductivity, refractive index, mechanical and magnetic properties. Therefore these materials permeate several fields, for example, catalytic processes, data storage, and sensors [1-3]. Among the nanostructure materials, simple and mixed metal oxides draw attention in several fields due to their special properties as excellent chemical stability and mechanical hardness [4-8].

Copper and/or cobalt oxides have been investigated in different applications such as solar cells, Li batteries, catalysis, sensors, and super capacitors based on the excellent properties. The interesting optical characteristics in the near and visible range were observed and can calculate the band gap energies of these oxides [9-20]. In addition, spinel cobalt oxide (Co_3O_4) is an essential magnetic semiconductor with band gap energy of 1.5eV [16]. The cobalt oxide (Co_3O_4) with a normal spinel structure is a mixed-valence compound, CoO,

*) **Corresponding author:** amn341@yahoo.com

Co_2O_3, leading to more applications. This observation enabled most researchers to fabricate different resources based on cobalt via substitution of CoO by any divalent element. In fact, the solid-solid interaction between two or more oxides leads to important products with certain physicochemical properties that differ from that for individual oxides. The spinel Co_3O_4 allows us to replace the divalent cobalt cations with other metal cations such as divalent metal cations leading to the formation of various cobaltite spinels such as copper cobaltite, $CuCo_2O_4$ [21].

Several synthetic techniques were reported for the preparation of different crystalline metal composites such as precipitation, sol gel, microwave co-precipitation, combustion, thermal oxidation, and sonochemical routes [22]. Most of these methods require high temperature conditions and the yielded particles had asymmetrical shape and size [23]. However, the combustion methods are favorable due to their convenience and speed in the production of different nanomaterials [24-26].

Spinel $CuCo_2O_4$ crystals with dissimilar morphologies have been prepared via one step hydrothermal method by using different precursors [27]. The authors claimed that a chrysanthemum-like $CuCo_2O_4$ crystal and a rose-like $CuCo_2O_4$ crystal were obtained by using Cu-Co chlorides and nitrates, respectively. The different morphologies of the as synthesized materials brought a better super capacitive performance. However, Ni and Mg cobaltite spinels were synthesized via a green chemical approach by using pomegranate fruit peel extract as fuel, in household microwave oven by solvent combustion process [28]. These authors display the formation of $NiCo_2O_4$ and $MgCo_2O_4$ spinels with the presence of some impurities of Ni and Mg oxides, respectively.

The objective of this paper is to synthesize $CuO/CuCo_2O_4$ nanoparticles using the auto combustion method in presence of urea. FTIR, SEM/EDX, and TEM/SAD techniques were used to characterize the prepared nanoparticles. The optical properties were studied by UV-visible spectra. The electrical properties of S1, S2 and S3 the synthesized nanoparticles were determined by using DC and AC electrical conductivity and dielectric measurements.

2. Materials and Experimental Procedures

2.1 Materials

The chemical materials were cobalt (II) nitrate hexahydrate, copper (II) nitrate hexahydrate and urea with linear formula $Co(NO_3)_2{\cdot}6H_2O$, $Cu(NO_3)_2{\cdot}3H_2O$ and H_2NCONH_2, respectively. These reagents were of analytical grade supplied by Sigma-Aldrich Company and used without further purification.

2.2 Preparation of cobaltite materials

Series of $CuO/CuCo_2O_4$ composites were synthesized by mixing calculated proportions of cobalt and copper nitrates with a definite amount of urea. The precursors were concentrated in a porcelain crucible on a hot plate. The water of crystallization was vaporized at 80^{o}C yielding a voluminous and gel product and then formed the combusted powders in the container by rising the heat temperature to 350^{o}C. The obtained powders were burned out in the air at 750^{o}C for 3h**.** The process flowchart for the synthesis of different composites is illustrated in Fig. 1. Ratios of Cu/Co were 0.25, 0.5 and 0.75 for S1, S2 and S3 samples, respectively.

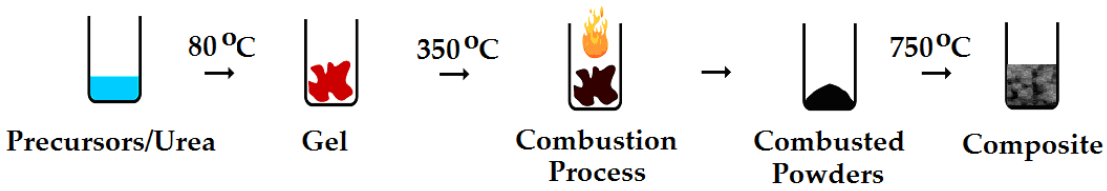

Fig. 1. Process flowchart for synthesis of different composites.

2.3 Characterization techniques

An X-ray diffraction measurement (XRD) of the prepared nanoparticles was carried out using a BRUKER D8 advance diffractometer (Germany). The patterns were run with Cu K_α radiation at 40 kV and 40 mA with scanning speed in 2θ of 2°min^{-1}. The crystallite sizes of crystalline phases of the solids calculate according to Scherer equation [28].

$$d = \frac{B\lambda}{\beta \cos\theta} \qquad (1)$$

where d is the average crystallite size, B (0.89) is the Scherer constant, λ is the wavelength of X-ray beam, B is the full-width half maximum (FWHM) of diffraction, and θ is the Bragg's angle. The lattice density is determined from the relation:

$$D_x = ZM/NV \qquad (2)$$

where Z is the number of molecules per unit cell, N is Avogadro's number, M is the molecular weight, and V is the volume of the unit cell.

Fourier-transform infrared spectroscopy (FTIR) was determined using Perkin-Elmer Spectrophotometer (type 1430) from 4000 to 400 cm^{-1}. The sample disks were placed in the holder of the double grating IR spectrometer.

Scanning electron micrographs (SEM) and high-resolution transmittance electron microscope (HRTEM) images were recorded on both a JEOL JAX-840A electron micro-analyzer and JEOL Model 1230 (Jeol, Tokyo, Japan), respectively. Additional analysis for the prepared solids carried out by using selected area electron diffraction (as SAD or SAED).

The energy-dispersive X-ray analysis (EDX) was recorded on a JEOL (JED-2200 Series) electron microscope with an attached Kevex Delta system.

2.4 Optical measurements

The ultraviolet-visible absorption spectra (UV-Vis.) of the prepared samples were measured using JASCO corp. V-570 spectrophotometer over the spectral range from 200 to 800 nm with an accuracy of ±0.1 nm. The optical band gap energy E_g of the prepared nanoparticles was estimated from Tauc equation [29].

$$(\alpha h\upsilon)^n = A\,(h\upsilon - E_g) \qquad (3)$$

where n is either 2 for direct transition, or 1/2 for an indirect transition, depending on the nature of possible electronic transitions, α is absorption coefficient, A is proportionality constant, h is Planck's constant, and υ is the frequency of the incident photon. In the Tauc equation, the plot of $(\alpha\, h\upsilon)^2$ against photon energy (hυ) for the investigated sample leads to the design of a certain curve, the intersection of the extrapolated linear portion of this curve with the (hυ) axis brought about the value of the optical band gap.

2.5 Electrical measurements

The electrical properties of the prepared nanoparticles are of great importance in determining whether it is matching with our necessities or not. Conductivity (DC and/or AC) is an important factor that reveals essential and reliable information about the transport phenomena. The electrical properties of the prepared samples were investigated using RLC Bridge (HIOKI model 3532, Japan) from 303 to 463 K at different frequencies ranged from 100 Hz to 8 MHz. The prepared samples as a disc were placed between the two electrodes. A programmable automatic RLC bridge was used to measure the capacitance C and the loss tangent tan δ directly. The DC electrical measurements have been carried out in a vacuum of 10^{-3} Torr in a specially designed holder. The electrical conductivity σ_{dc} was determined using the following equation:

$$\sigma = \frac{d}{R_p a} \qquad (4)$$

where d is the thickness, a is the cross sectional area and R_p is the resistance. Then the activation energy E_g calculates from Arrhenius equation:

$$\sigma_{dc}(T) = \sigma_o \exp\left(-\frac{\Delta E_a}{KT}\right) \qquad (5)$$

where σ_o is the proportional constant, k is the Boltzmann constant, and T is the temperature. It is well known that the AC conductivity, σ_{ac}, depends on the frequency and temperature and it can be represented as the sum of two terms:

$$\sigma_{ac}(\omega) = \sigma_{tot}(\omega) - \sigma_{dc}(T) \qquad (6)$$

where $\sigma_{dc}(T)$ is DC electrical conductivity and $\sigma_{Tot.}(\omega)$ is the total electrical conductivity. The term $\sigma_{ac}(\omega)$ can be written in the form of Jonscher power law as [30]

$$\sigma_{ac}(\omega) = A\omega^S \qquad (7)$$

where $\omega = 2\pi f$ is the angular frequency, and A and s are composition-dependent parameters. The values s were obtained from the slope of these lines [31].

Another essential set of properties of semiconductor material are the dielectric properties. In this study, the dielectric constant ε′ calculates from the measured capacitance at all temperatures and frequencies according to the following equation [32]:

$$\varepsilon' = \frac{C_p d}{A \varepsilon_o} \qquad (8)$$

where ε_o is the permittivity of a free space (ε_o=8.85×10^{-12} F/m).

3. Results and Discussion

3.1. Structural analysis

The patterns of XRD for $CuO/CuCo_2O_4$ powders are illustrated in Fig. 2. This figure shows the formation of powders (S1, S2, and S3) containing CuO and $CuCo_2O_4$ crystals. Diffraction peaks at 2θ =18.94°, 31.20°, 36.79°, 38.73°, 44.77°, 53.73°, 55.56°, 59.35°, 65.16°, 68.10° and 77.21° are characteristic to indexing planes (111), (220), (311), (222), (400), (422),

(511), (440), (531) and (533), respectively. This agrees with the values reported for $CuCo_2O_4$ (JCPD file No. 01-1155). Another series of diffraction lines at 2θ =32.54°, 35.35°, 38.51°, 46.17°, 48.59°, 53.73°, 58.20°, 61.47°, 65.19°, 68.12°, 72.12° and 75.24° are characteristic to indexing planes (110), (-111), (111c), (112), (202), (020), (202), (-113), (022), (220), (311) and (004), respectively. This agrees with the values reported for CuO (JCPD file No. 41-254).

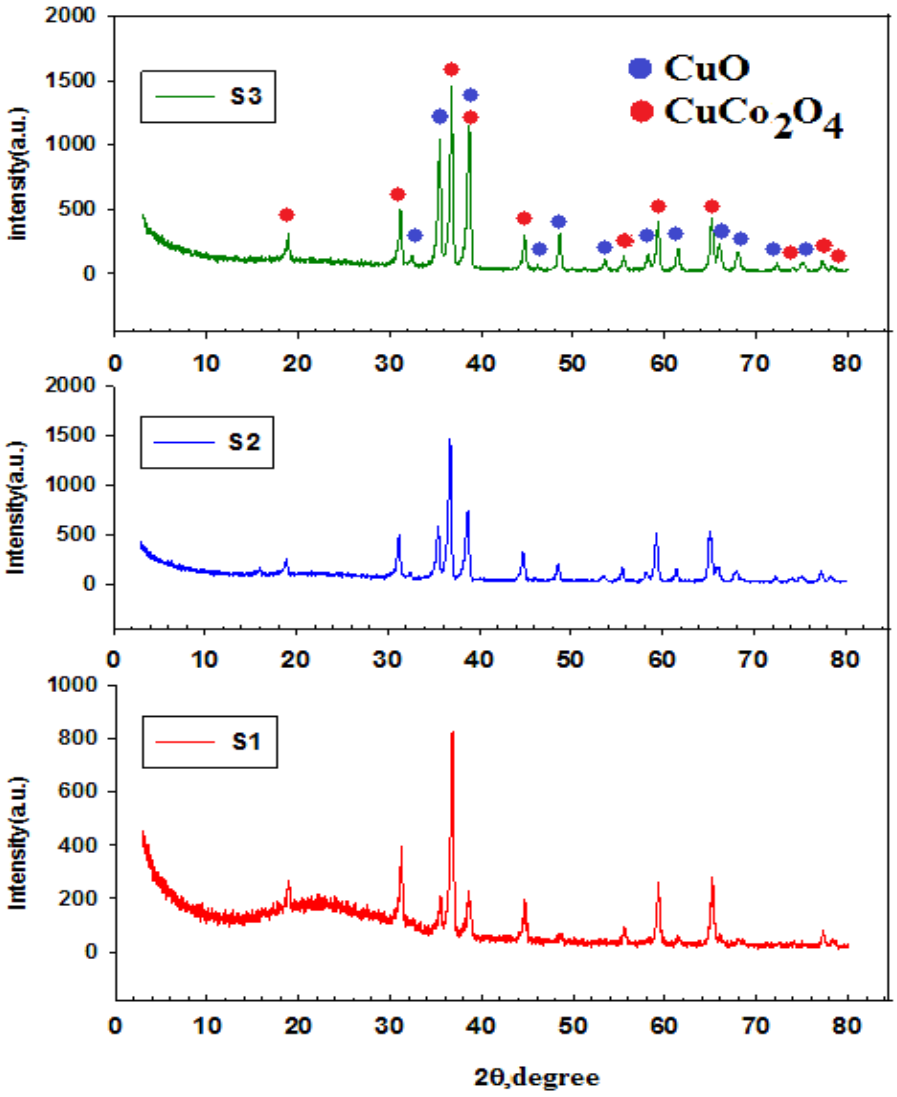

Fig. 2. XRD patterns for the S1, S2, and S3 samples.

From XRD patterns, it was found that the cubic spinel-type structure for $CuCo_2O_4$ is the major phase and monoclinic CuO is a minor phase. In detail, it was observed that the peaks of $CuCo_2O_4$ (311) shift to a higher Bragg's angle with increasing copper concentration revealing the enhancement formation of $CuCo_2O_4$ with the subsequent presence of CuO. Also, the height of the characteristic diffraction lines of $CuCo_2O_4$ (311) and CuO (-111) planes, which are listed in Table I, can be used to calculate the relative contents for these oxides. The fraction (*F*) of the CuO phase in the as prepared $CuO/CuCo_2O_4$ composites can be determined using the relation:

$$F = I_{monoclinic}/I_{total} \quad (9)$$

where $I_{monoclinic}$ is the count of $I_{(-111)}$ of monoclinic CuO phase and I_{total} is the sum of the counts of $I_{(311)}$ and $I_{(-111)}$ for $CuCo_2O_4$ and CuO phases, respectively. The fractions of CuO phase were 18.99, 27.76 and 41.81 %, in the S1, S2, and S3 samples, respectively.

Tab. I Some peak height for CuO and $CuCo_2O_4$ involved in the as prepared samples.

Samples	Peak height (a.u.)				
	CuO	$CuCo_2O_4$			
	I_{-111}	I_{311}	I_{220}	I_{551}	I_{440}
S1	192	819	240	193	223
S2	568	1478	399	434	506
S3	1045	1454	389	350	396

The (220) and (440) planes, the intensities increase as the amount of copper increases, enabling us to shed light on the cations in the tetrahedral (A) and octahedral (B) sites, respectively [24,25]. The intensities of these planes infer that the Cu^{2+} and Co^{3+} ions occupied both the A and B sites. In addition, estimation of the different structural parameters of cubic spinel $CuCo_2O_4$ such as (A–O and B–O) bond lengths, (r_A, r_B) ionic radii, and the distance between the reacting ions (L_A and L_B). The structural parameters values of the prepared $CuCo_2O_4$ were listed in Table 3. It is found that the rise of the copper content led to a decrease in L_A, L_B, r_A, r_B, A–O and B–O values, the crystallite size (d), unit cell volume (V), lattice constants values (a), and micro-strain of the prepared copper cobaltite nanoparticles. The lattice parameter calculates to be 0.8108 nm, which is quite close to the reported values by Chi et al [33,34].

Tab. II Structural parameters of the prepared copper cobaltite included in different prepared solids.

parameter	S1	S2	S3
d (nm)	37	34	32
a (nm)	0.8107	0.8105	0.8094
V (nm^3)	0.5328	0.5325	0.5303
D_x (g/cm^3)	6.117	6.120	6.146
ρ_d	7.305×10^{-4}	8.651×10^{-4}	9.766×10^{-4}
Strain	0.3303	0.2720	0.2137
L_A	0.3510	0.3509	0.3505
L_B	0.2865	0.2864	0.2860
A–O	0.1853	0.1853	0.1853
B–O	0.2092	0.2091	0.2088
r_A	0.0533	0.0533	0.0530
r_B	0.0772	0.0771	0.0768

However, it can be seen from Table III that there is a dislocation of $CuCo_2O_4$ particles. Indeed, the dislocation resulted in a distortion in the regular atomic array of a perfect crystal [35-37]. The solid-solid interaction of CuO and Co_3O_4 resulted in the formation of copper oxide substituted cobaltic oxide ($Cu_xCo_{3-x}O_4$) system. It is assumed that the presence of solid-state products with individual oxide will lead to synergistic effects that may help to improve the properties of the synthesized materials. The concentration of the individual elements of the cobaltite affects the thermal diffusion of Co and Cu cations through the early copper cobaltite which covers the surfaces of CuO and Co_3O_4 grains. However, oxygen vacancies

may be formed via the dissolution of copper ions in the lattices of cobalt enhancing the mobility of cobalt and copper cations with subsequent stimulation of $Cu_xCo_{3-x}O_4$ formation. The proposed mechanism of cobaltite formation is as follows:

At Co_3O_4 interface:

$$Co_3O_4 + Cu^{2+} \rightarrow CuCo_2O_4 + Co^{2+} \quad (10)$$

At CuO interface:

$$2Co^{2+} + CuO + 1.5\ O_2 \rightarrow CuCo_2O_4 \quad (11)$$

The diffusion of $Cu^{2+}$and Co^{2+} through relatively rigid cobaltite film resulted in enhancement formation of $CuCo_2O_4$ particles due to an increase of the contact surface area between the reacting ions [38]. The enhancement effect of the CuO on copper cobaltite formation can be determined by measuring the height of diffraction lines characteristic for $CuCo_2O_4$ d-spacing (0.244 nm 100 %) [37]. Before the stoichiometry content of $CuCo_2O_4$, the increase in the amount of CuO resulted in an increase in thepeak height of $CuCo_2O_4$.. Opposite behavior was observed with any excess amount of copper oxide after the stoichiometry content of $CuCo_2O_4$ due to contraction of the as prepared cobaltite depending on incorporation of some copper ions in its crystal lattice [39].

3.2. Fourier-transform infrared spectroscopy (FTIR)

Fig. 3 shows the FTIR spectra of the prepared composites S1, S2, and S3 recorded between 4000 and 400 cm^{-1}.

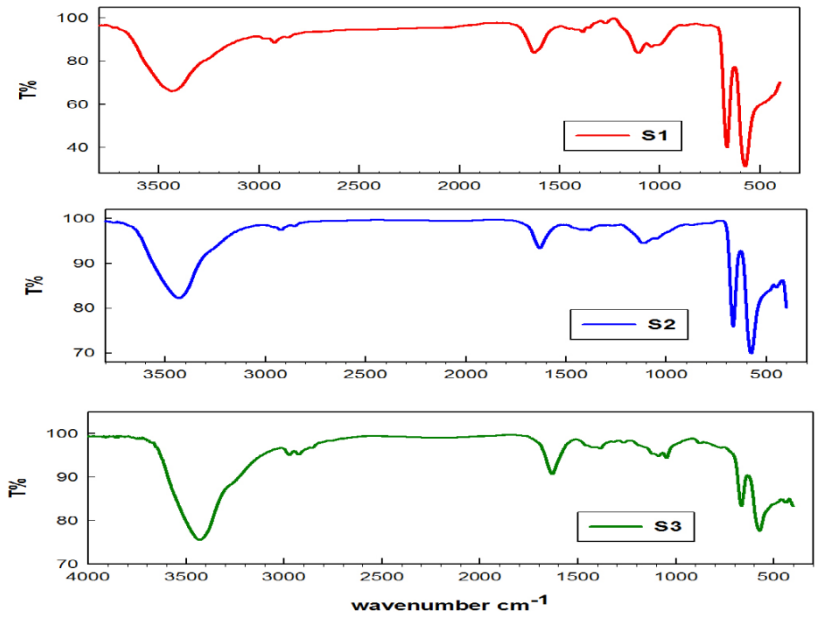

Fig. 3. FTIR spectra for the S1, S2, and S3 samples.

The spectra explain the position, vibration modes and crystal structure of the ions. Generally, the cobaltite crystallizes in a spinel structure with the space group *Fd*3*m*. In fact, the spinel cobaltite is known to exhibit two IR active modes in the band around 600 cm^{-1} for the tetrahedral A site, and in another band around 400 cm^{-1} for the octahedral B site. In this study, two sharp bands were observed at 666–664 cm^{-1} and 576–572 cm^{-1} with a shift towards the higher wavelength by increasing copper content. This shift result from the rearrangement of Cu species in the cubic spinel structure [40,41].

In addition, the broad band at 3438–3429 cm^{-1} and at 1271–1048 cm^{-1} could be ascribed to the normal O–H stretching vibration of H_2O in the Cu–Co–O lattice indicating that the nano crystalline materials show a high surface to volume ratio and thus absorb moisture [42]. Another sharp band located at 1631–1627 cm^{-1} referred to H–O–H bending vibration, which was assigned to a small amount of H_2O in the CuO nanocrystals [43]. However, the augmentation in the copper content showed a slight shift in the position and also an increase in the intensity of previous bands. This observation could be attributed to the quantum size and surface effects of nanoparticles [44].

From XRD and IR results it is found that the cation distribution in $CuCo_2O_4$ can be discussed in light of preferential occupation for the cation in certain sites in the spinel structure. in fact, Cu^{2+} ions have occupied the octahedral (B) site while Co^{3+} ions have occupied both the tetrahedral and octahedral sites [37, 45]. However, the incorporation of Cu in the spinel $CuCo_2O_4$ resulted in the substitution of some Co^{2+} located at B site by Cu^{2+} with subsequent transformation of Co^{2+} to Co^{3+}, then movement to A sites. These processes led to a decrease in both size and lattice constant of $CuCo_2O_4$ due to the variation in the ionic radii of Cu^{2+} (0.069 nm), Co^{2+} (0.078 nm), and Co^{3+} (0.063 nm). In contrast, CuO action brought about an increase in the X-ray density of copper cobaltite due to the higher atomic weight of Cu than that of Co. These data are tabulated in Table II.

The maximum intensity of (220) and (440) planes are 66.2 and 117.2 %, respectively. This confirms that the incorporation of copper at B sites is greater than that at A sites. The Cu–O and Co–O in the B-site are different from those in the A-site due to the difference in the mass and charge of Cu^{2+} ions and that of both Co^{2+} and Co^{3+} ions [46]. The band corresponding to the octahedral region contains two bands. The splitting of octahedral bands is due to the difference in the mass of the octahedral (Cu^{2+} and Co^{3+}). If only the Co^{3+} ions had been observed at the B site, the octahedral band would have been single. Similar results were observed in the nickel cobaltite system fabricated by using a co-precipitation route [47]. The previous findings confirm migration of some Cu^{2+} ions from B to A-site with the speculated formula as following:

$$(Cu_y^{2+}\ Co_x^{3+})_A\ [Cu_{1-y}^{2+}\ Co_{1-x}^{2+}\ Co^{3+}]_B\ O_4^{2-} \qquad (12)$$

This indicates that the synthesized copper cobaltite has a partially inverse or random spinel structure. In addition, this depends on the preparation method and the coexistence of CuO with $CuCo_2O_4$. However, the data was observed in Table II confirms this speculation about cation distribution in the as synthesized copper cobaltite nanoparticles.

3.3. Morphological and elemental analyses

Investigation of the copper content on the morphological and elemental composition of the as prepared powder carried out by using SEM, HRTEM, SAED, and EDX techniques whereby completely different morphologies were obtained with each one.

Fig. 4 displays SEM images of S1, S2, and S3 samples. It is clear from this figure that different samples consisted of polyhedral, compact granular, and agglomerated spherical-like structures with well dispersing coexists. In addition, the characterization of the chemical composition with energy-dispersive X-ray spectroscopy (EDX) can be illustrated in Fig. 4. It was found that our samples consisted of Co, Cu, and O elements confirming the preparation method is authentic. This figure showed an overall Cu: Co atomic ratio with various changes according to the copper content. However, the S2 sample showed an overall Cu: Co atomic ratio close to 1:2, in harmony with the stoichiometry of the $CuCo_2O_4$ compound.

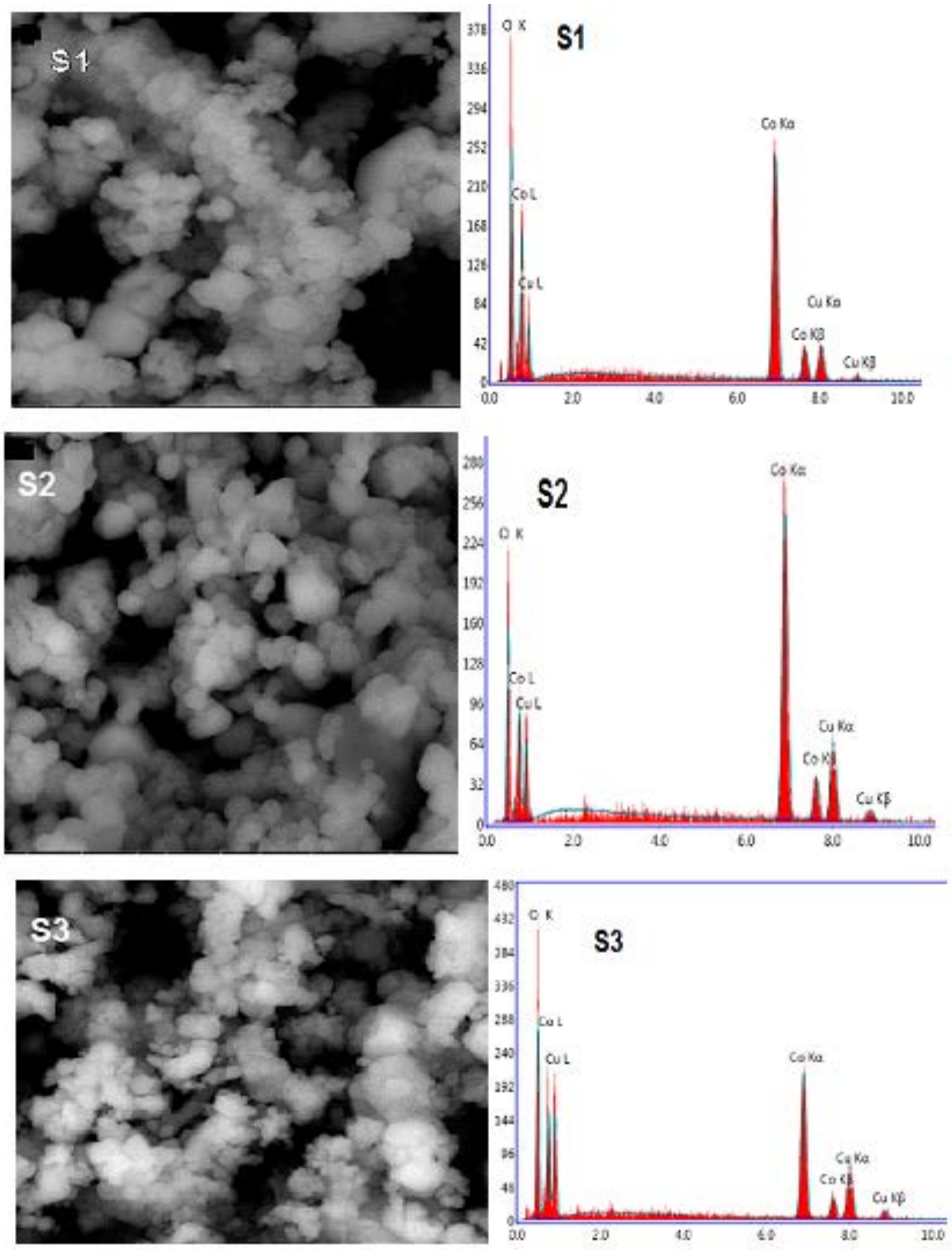

Fig. 4. SEM images and EDEX for the S1, S2, and S3 samples.

Different structures of the porous nanoparticles were clearly revealed by HRTEM analysis as shown in Fig. 5. Voids and pores can be found on the prepared solid surface due to the liberation of gas molecules during the decomposition of the copper-cobalt precursors. Fig. 5 manifests the different nanostructures, which agree with the SEM. However, the spherical nanoparticles were aggregated together into a bundle like structure as shown in the S3 sample. The increase in copper content led to the rod-like morphology formed by the small spherical shape particles. In addition, this treatment resulted in a slight reduction in the size of particles. This observation has coincided with the XRD data in this study. Moreover, the continuously selected area electron diffraction SAED ring patterns embedded with large spots reveal the crystalline nature of the nanoparticles as represented in Fig. 5. This figure consisted entirely of ring patterns of multiple crystals with variable orientation. This observation confirms the polycrystalline nature of the synthesized samples [48]. However, increasing the

copper content led to a rise in the spots in SAED patterns as shown in the S3 sample. It seems that the observed morphological differences could be attributed to the different growth and/or agglomeration mechanisms brought about depending on the increase in copper content.

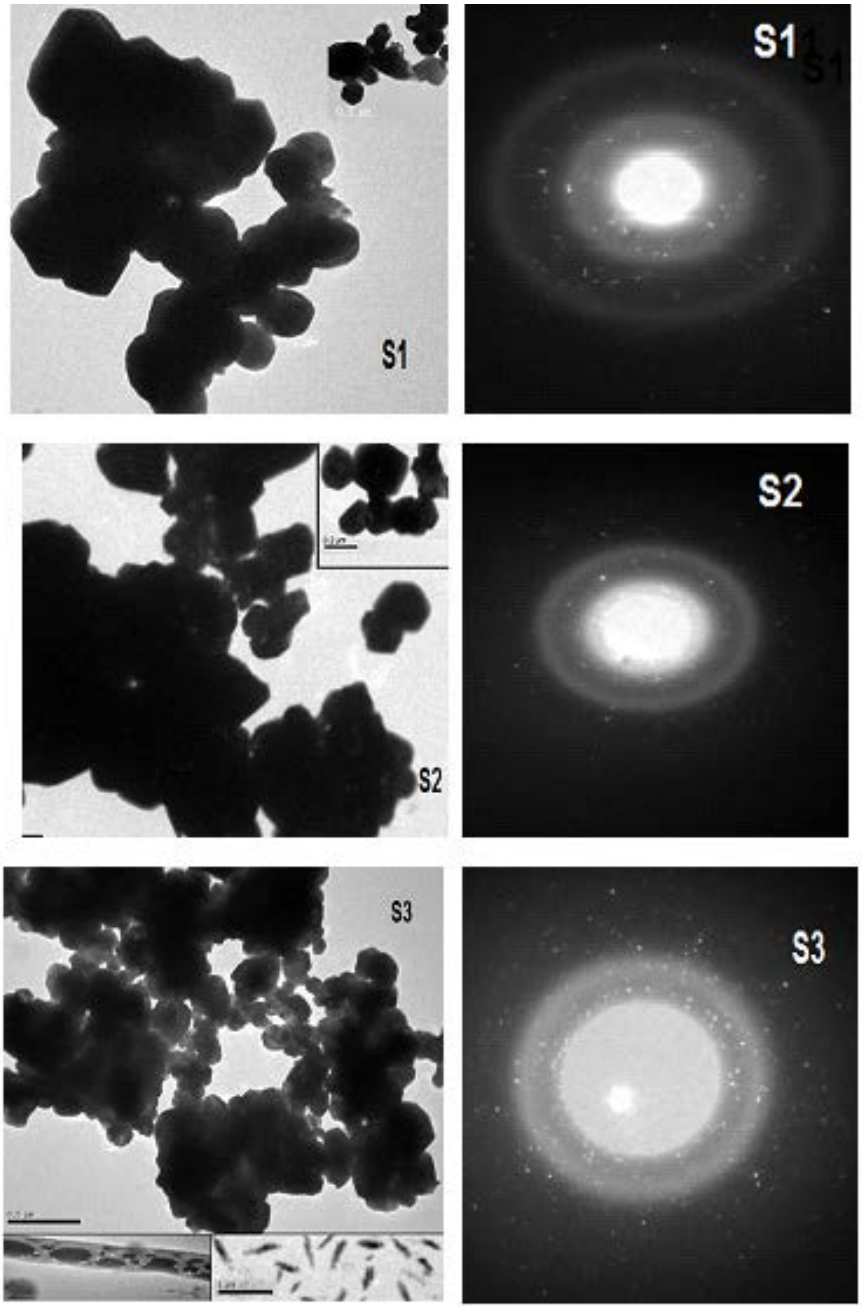

Fig. 5. TEM images and diffraction patterns of the S1, S2, and S3 samples.

3.4. Optical properties

The optical properties of S1, S2, and S3 nanoparticles were analyzed by absorption spectra obtained from UV-visible spectroscopy to visualize the effect of the structure and copper content on the optical properties of $CuO/CuCo_2O_4$ nanoparticles. The copper cobaltite has a dark color; a broad absorbance peak can be seen in Fig. 6.

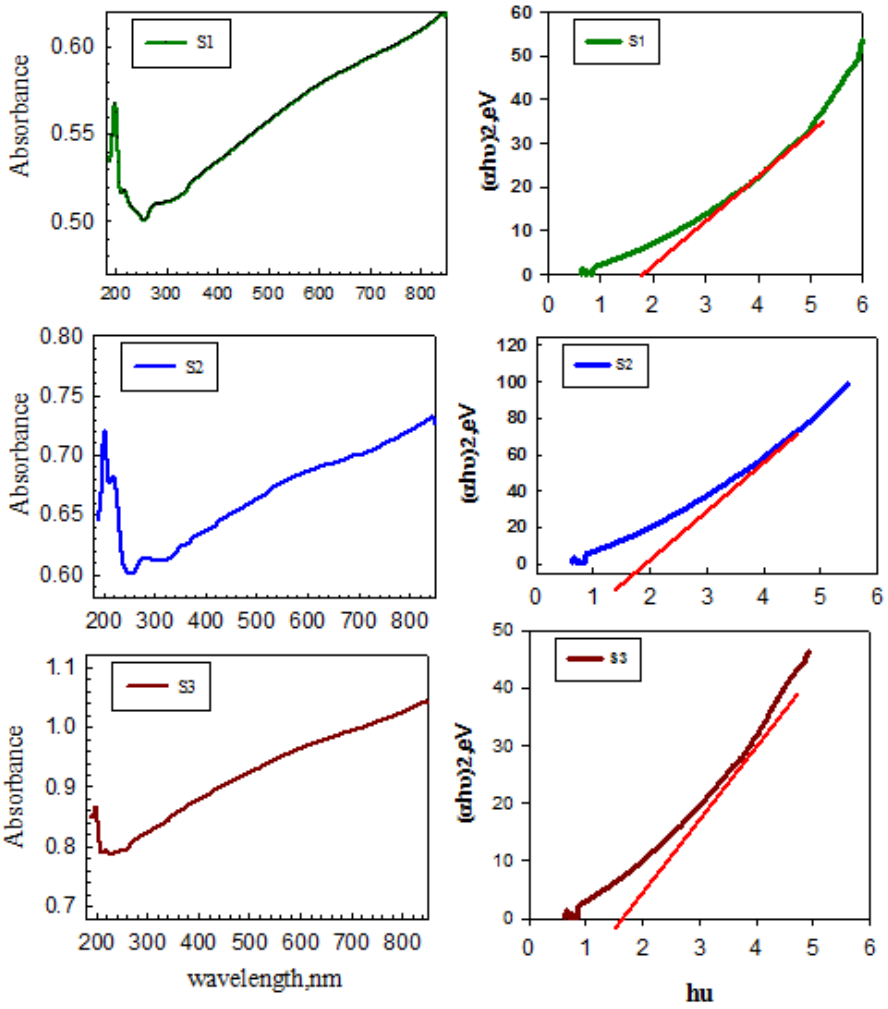

Fig. 6. UV–visible spectra and $(\alpha h\nu)^2$ Versus hν for the S1, S2 and S3 samples.

The optical band gap E_g values calculate from Tauc equation (3), by the intersection of the extrapolated linear part of the plot $(\alpha\ h\upsilon)^2$ against (hυ) Fig. 6. The optical band gap energies for S1, S2, and S3 are 1.8, 1.5, and 1.2 eV, respectively, which is in good agreement with the previous report [49]. The band gap of copper cobaltite is 2-2.2 eV and it takes a lower value in presence of CuO. The values of E_g depend on both the crystal structure and phase composition of the investigated material. It can be seen that an increase in copper content led to a decrease in E_g due to the formation of local levels [50]. The lower band gap could lead to better mobility of lattice oxygen with a subsequent enhancement for electrical properties and conductivity of copper cobaltite depending upon the existence of half-filled d-orbital of Co^{3+}. From XRD data, the electron configuration in the nanoparticles $CuCo_2O_4$ is the tetrahedral high spin Cu^{2+} with octahedral low spin Co^{3+}. The energies can be attributed to the O^{2-}2p orbital as the valence band and octahedral ions Co^{3+} and Cu^{2+} 3d orbital as the conduction band [51].

3.5. Electrical characteristics of the nanoparticles

The electrical characteristics are significance in determining whether the material is matching our requirements or not. The conductivity is an essential factor that reveals essential information about the performance of electric charge carriers to understand the conduction

mechanism. The changes in the electrical properties may be attributed to the effective role of composition, porosity, and grain size. Investigation of the frequency dependence of the electrical properties in the investigated temperature range led to the operating conduction processes. In order to emphasize this point and get information about the operating conduction mechanisms, electrical properties as the DC and AC electrical conductivity, and the dielectric constant were studied.

3.5.1. DC electrical conductivity

Variation of the resistance of the prepared samples with the temperature was studied. Fig. 7 shows this variation of resistance of the S1, S2, and S3 samples in the temperature range 298-463 K. This figure revealed that the resistance of the prepared samples decreases with increasing of temperature due to a decrease in the oxygen vacancy. Also, the resistance decreases with increase in the Cu content and copper-rich sample S3 has the lowest values of resistance at all temperatures range.

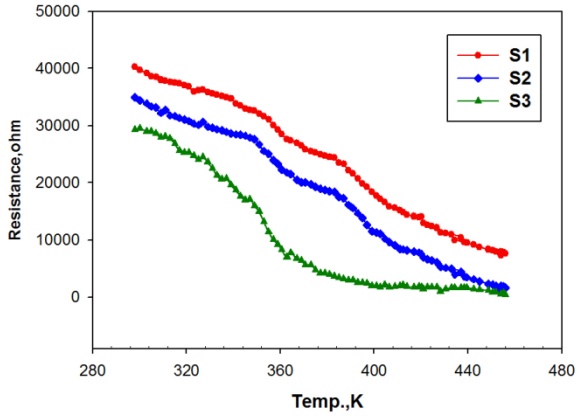

Fig. 7. Variation of resistance with temperature of S1, S2 and S3 samples.

The DC electrical conductivity, σ_{dc}, was predictable from the resistance according to equation (4). Fig. 8 displays the variation of the DC electrical conductivity with temperature in the range from 298 to 463 K via the plots of Log σ_{dc} versus $10^3/T$ for synthesized nanoparticles. The figure shows that the σ_{dc} values increase as the content of copper and/or temperature increase. According to Arrhenius, equation (5), the plots enable us to estimate the activation energies of different samples.

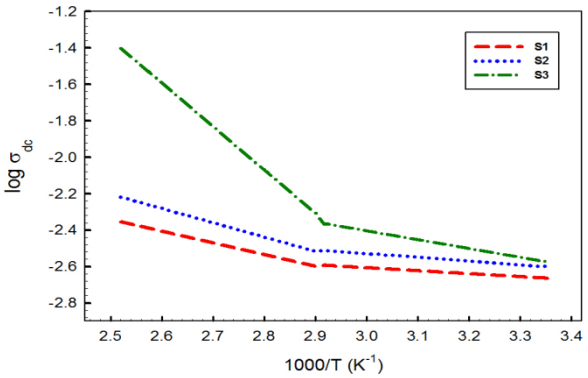

Fig. 8. Temperature dependence of dc-conductivity for S1, S2, and S3 samples.

In Fig. 8, two regions were observed with different activation energies (ΔE) due to the occurrence of two components (CuO and $CuCo_2O_4$) in each sample. Region I or low-temperature range (298-375 K) give ΔE_I between 0.09 eV and 0.031 eV and region II or high-temperature range (375-463 K) with ΔE_{II} between 0.34 eV and 0.18 eV for various samples. These results reveal that the conductivity of $CuO/CuCo_2O_4$ nanoparticles could be attributed to ionic conduction region II and electronic conduction region I. In addition, the low values of the activation energy in both regions I and II indicate that the prepared nanoparticles are semiconducting materials.

3.5.2. AC electrical conductivity

The variation of the AC conductivity (σ_{ac}) of the S1, S2, and S3 prepared samples as a function of frequency and temperatures are illustrated in Fig. 9.

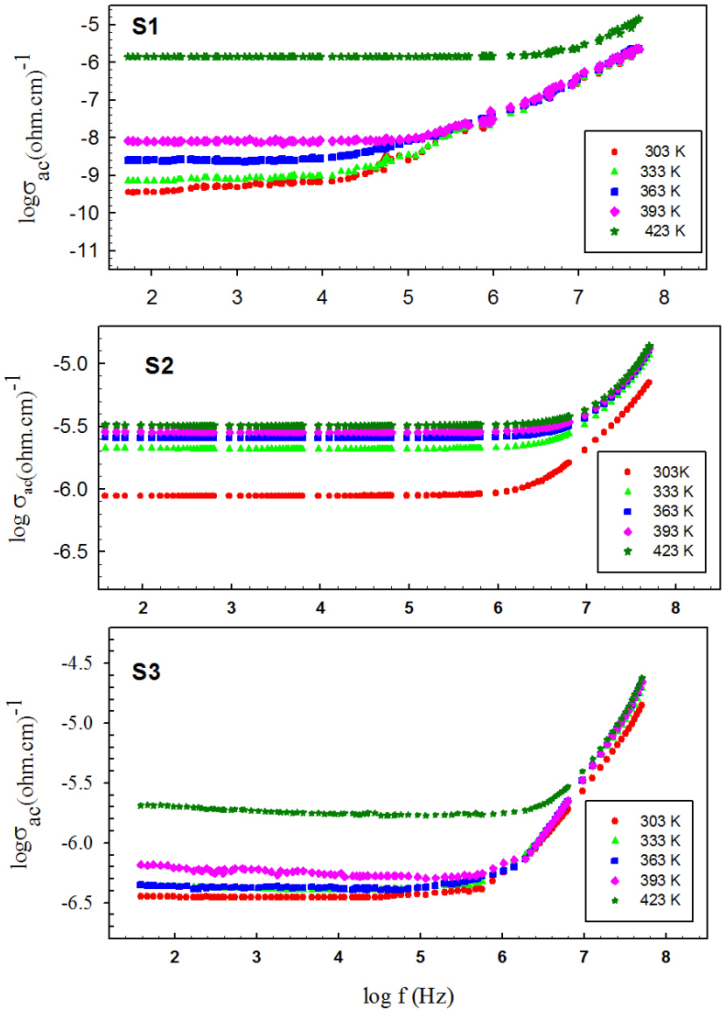

Fig. 9. Frequency dependence of AC electrical conductivity for S1, S2, and S3 samples.

The general view of this figure shows that a plateau region corresponds to σ_{dc} at low frequencies. The maximum electrical conductivity of the prepared samples is $1.5x10^{-5}$, $1.9x10^{-5}$, and $2.5x10^{-5}$ at 423 K, in the order S3 > S2 > S1. At the high-frequency range, the electrical conductivity increases and merges into a single curve with increasing temperature.

Hence, the difference in the conductivity disappears and shows nearly equal values. The conductivity could be attributed to the relaxation phenomena of the ionic atmosphere which arises from the mobile charge carriers.

In general, the electrical properties of the semiconductors depend onthe valancy , concentration and mobility of elements of its formation.. The results in this study showed that the conductivity of the various samples has been explained by three terms: (i) the interstitial oxygen ionic migration, (ii) hopping behavior, and (iii) the cation distribution.

In fact, the oxygen vacancies are considered as one of the mobile charge carriers in oxide-ion conductors. However, at high temperatures, the decrease in the activation energy and increase in the conductivity is attributed to an order/disorder transition of the oxygen vacancies

The conductivity of copper cobaltite can be explained by Verwey–de Boer model which depends on hopping actions [52]. The hopping of electrons and holes is more possible at B sites compared to that at A sites because the distance between the metal ions at the B sites (0.2865–0.2860 nm) is smaller than the distance at A sites (0.3510–0.3505 nm) as listed in Table III. The conduction mechanism in $CuCo_2O_4$ can be represented as $Cu^{+} + Co^{3+} \leftrightarrow Cu^{2+} + Co^{2+}$, wherein electron hopping occurs via $Co^{3+} \leftrightarrow Co^{2+}$ and hole hopping via $Cu^{2+} \leftrightarrow Cu^{+}$. Moreover, the conductivity increases with temperature due to the thermal activation of the drift mobility of charge carriers according to the hopping model [53-55].

As reported former, a cation site preference in the as synthesized $CuCo_2O_4$ has been seen with the Co^{2+} ions occupying the B-sites while the Cu^{2+} and Co^{3+} ions are dispersed among both A- and B-sites. However, XRD measurements refer to the conversion of Co^{3+} to Co^{2+} by increasing copper content with subsequent change in the cation distribution of spinel structure. A corresponding increase in conversion of Co^{3+} to Co^{2+} increases in conduction electrons, so the conductivity increases with the increasing copper content.

By applying Jonscher equation 7 "s" values were determined from the slope of straight lines of the relation of conductivity with frequency "s" values decreasing with the rising temperature as shown in Fig. 10. In our study, "s" values are less than 1 for all temperatures [56]. This finding confirms that mechanism of Ac-electric conductivity for the as synthesized composites can be attributed to the hopping conduction of charge carriers [57, 58]. Where, values of "s" are the frequency exponent which changes in the range from 0 to 1 representing the degree of interaction between mobile ions and its surrounding [59].

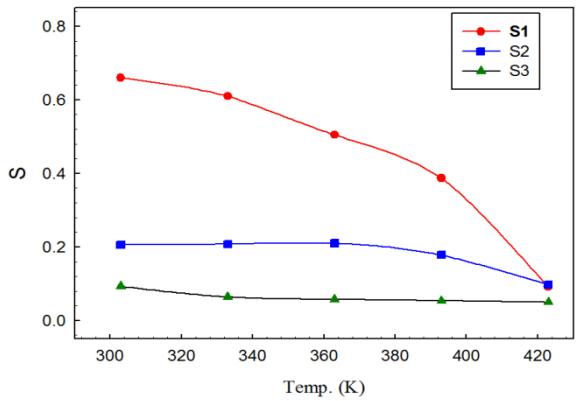

Fig. 10. Variation of "s" values with temperature for S1, S2, and S3 samples.

3.5.3. Dielectric properties

The dielectric measurements expose insight into the performance of electrical charge carriers. The effect of temperature and frequency on the dielectric constant ε' and tan δ of the

nanoparticles were studied. Variation of ε' for the S1, S2, and S3 nanoparticles at different temperatures in the frequency range 10^2–10^6 Hz is illustrated in Fig. 11. Investigation of this figure revealed that the values of ε' are $8.716x10^3$, $1.961x10^3$, and $1.4744x10^5$ at 100 Hz and at room temperature and decrease with increasing frequency as $1.980x10^3$, 1578, and 2661 at 1000 Hz for S1, S2, and S3 respectively and at high frequency ε' remains constant. At low frequencies, as the temperature increases, ε' increases for all samples. In other words, ε' depends on the temperature.

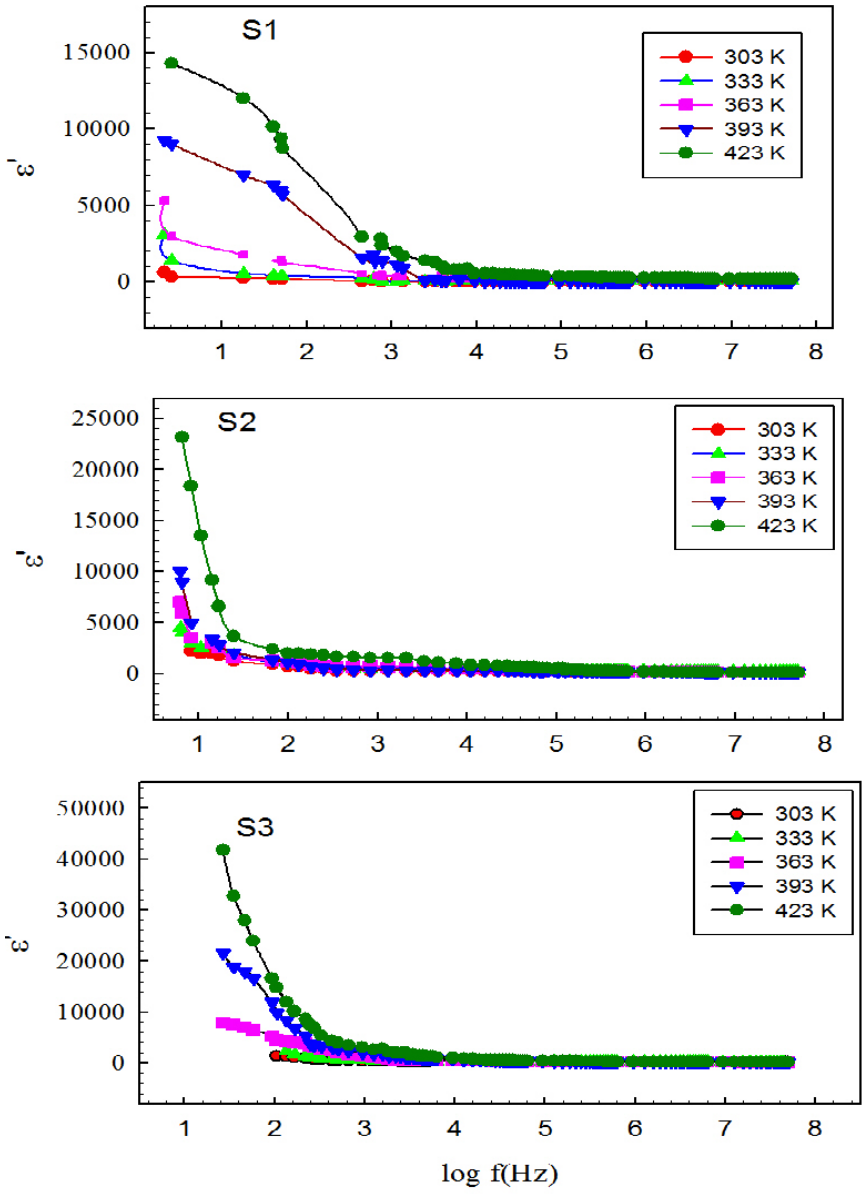

Fig. 11. The variations of dielectric constant (ε') with frequency at different temperatures for the S1, S2, and S3 samples.

Dielectric constant ε' can be discussed based on the polarization process. The observed ε' could be attributed to one the following factors; the contribution of ionic, electronic, dipolar, and interfacial polarization. At low frequencies, the polarizations are dipolar and interfacial; both of them are temperature dependent [60]. The crystal defect lead

to a decrease in dipolar polarization and an increase in interfacial polarization with increasing temperature [61]. This explains the high values of ε' at high temperatures and low frequencies. However, at high frequencies, ε' becomes almost temperature independent. This may be due to the dominance of the electronic and ionic polarization [60].

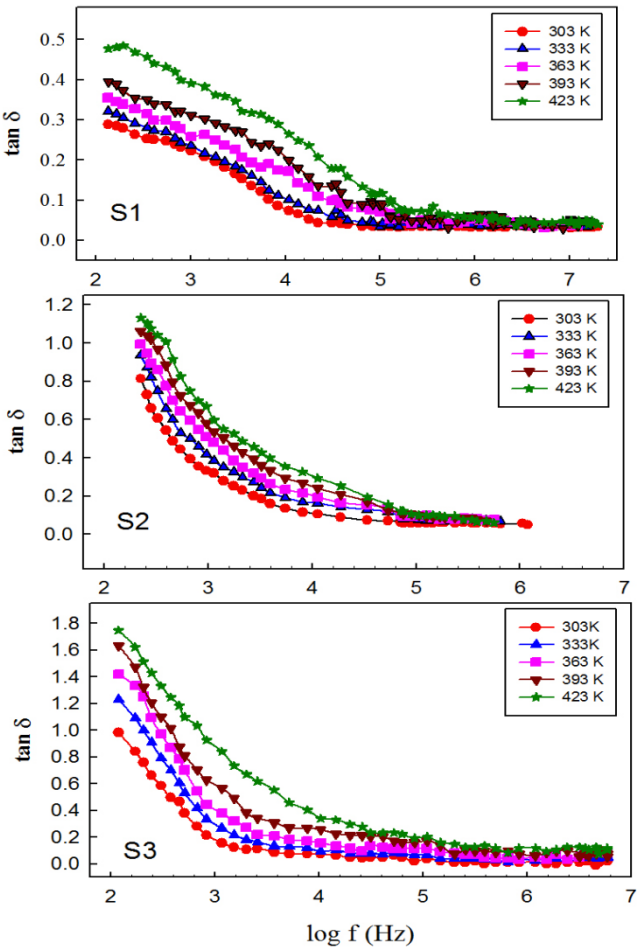

Fig. 12. Variation of tan δ with frequency at different temperatures for the S1, S2, and S3 samples.

The space charge or interfacial polarization dependence of dielectric dispersion for $CuO/CuCo_2O_4$ composites can be explained from the Maxwell–Wagner theory and Koops theory for inhomogeneous dielectrics [62-65]. Based on this model, the $CuO/CuCo_2O_4$ contains well-conducting grains (CuO and $CuCo_2O_4$) separated by grain boundaries. By applying an external field, the charge carriers within the grains migrate and accumulate at the grain boundaries. This high accumulation of the charge carriers causes large polarization and consequently high ε'.

The dipolar polarization in cobaltite can be attributed to the electron exchange between $Co^{3+}\leftrightarrow Co^{2+}$. The value of ε' decreases with frequency, becoming constant at high frequencies because the electronic exchange does not follow the external alternating field [66-68]. In addition, there are electronic and ionic polarization that contribute to the net polarization of the $CuO/CuCo_2O_4$. This polarization is due to the electron exchange between the presented cations ($Co^{3+}\leftrightarrow Co^{2+}$ and $Cu^{2+}\leftrightarrow Cu^{+}$) when an external electric field was applied.

The variation of the loss tangent (tan δ) with frequency at different temperatures of the $CuO/CuCo_2O_4$ system displays a normal behavior, as shown in Fig. 12. This figure revealed that tan δ decreases rapidly with increasing frequency, while in the high-frequency region it becomes frequency independent. Based on the discussion earlier, the fluctuation of the high resistive grain boundary is effective at low frequencies, and, therefore, greater energy is required for the electron exchange between $Co^{3+}\leftrightarrow Co^{2+}$ ions causing high losses. In the high-frequency region, which corresponds to low resistivity, the grains are more effective, and as a result smaller energy is required for the electron transfer between $Co^{3+}\leftrightarrow Co^{2+}$ ions. The loss tangent is also affected by numerous factors such as stoichiometry, Co^{2+} concentration, microstructural modifications, and cation distribution.

4. Conclusion

A series of $CuO/CuCo_2O_4$ composites was successfully synthesized via combustion method. XRD and FTIR results confirm the formation of spinel $CuCo_2O_4$ via solid-state reaction between copper and cobalt oxides. The change in the copper content resulted in various modifications in the morphological character of nanoparticles. Various prepared nanoparticles contain well dispersed particles with polyhedral, compact granular, and agglomerated spherical-like structures. The grains of the investigated composites did not exceed the nonmetric scale.

The calculated energy band gaps were 1.8, 1.5, and 1.2 eV for S1, S2, and S3 respectively. The coexistence of CuO and $CuCo_2O_4$ brought about a decrease in the energy band gap leading to good electrical properties of the investigated composites. The observed values confirm the semiconducting behavior of synthesized nanoparticles. The DC electrical conductivity of nanoparticles increases exponentially with the rising temperature. However, the increase in the copper content brought about a decrease in the activation energy. The decrease was more pronounced in S3 sample. So, it can be used in microelectronic devices. In addition, increasing frequency and temperature increases the AC electrical conductivity. The frequency exponent "s" decreases with temperature due to the correlated barrier hopping (CBH) mechanism.

The dielectric constant and loss tangent for all nanoparticles increase with increasing temperature and reduce with increasing frequency. The semiconducting behavior of copper cobaltite is inferred as the conductivity is found to increase with temperature. Thus, the nanograins of $CuCo_2O_4$ could suit well for semiconducting gas sensor applications by virtue of having easily hopping majority carriers.

5. References

1. P. R. Bandaru, C. Daraio, S. Jin, A. M. Rao, Novel electrical switching behaviour and logic in carbon nanotube Y-junctions, Nature materials, 4 (2005) 663-666.
2. L. Krusin-Elbaum, D. M. Newns, H. Zeng, V. Derycke, J. Z. Sun, R. Sandstrom, Room-temperature ferromagnetic nanotubes controlled by electron or hole doping, Nature, 431 (2004) 672-676.
3. J. Yang, J. B. Li, H. Lin, X. Z. Yang, N. Wang, X. G. Tong, Synthesis and characterization of regular hexagonal $NiCo_2O_4$ nanosheets, in, Trans Tech Publ, (2007) 2027-2029.
4. B. Ren, W. Shen, L. Li, S. Wu, W. Wang, 3D $CoFe_2O_4$ nanorod/flower-like MoS_2 nanosheet heterojunctions as recyclable visible light-driven photocatalysts for the degradation of organic dyes, Applied Surface Science, 447 (2018) 711-723.

5. C. R. Ravikumar, P. Kotteeswaran, A. Murugan, V. B. Raju, M. S. Santosh, H. P. Nagaswarupa, H. Nagabhushana, S. C. Prashantha, M. R. A. Kumar, K. Gurushantha, Electrochemical studies of nano metal oxide reinforced nickel hydroxide materials for energy storage applications, Materials Today: Proceedings, 4 (2017) 12205-12214.
6. S. Y. Tsai, C. T. Ni, K.-Z. Fung, Characterization of infrared transmittance in mixed transition metal oxides for solar cells application, Ceramics International, 43 (2017) S460-S463.
7. F. Falsafi, B. Hashemi, A. Mirzaei, E. Fazio, F. Neri, N. Donato, S. G. Leonardi, G. Neri, Sm-doped cobalt ferrite nanoparticles: A novel sensing material for conductometric hydrogen leak sensor, Ceramics International, 43 (2017) 1029-1037.
8. S. K. Shaikh, V. V. Ganbavle, S. V. Mohite, K. Y. Rajpure, Chemical synthesis of pinecone like ZnO films for UV photodetector applications, Thin Solid Films, 642 (2017) 232-240.
9. A. S. Zoolfakar, R. A. Rani, A. J. Morfa, A. P. O'Mullane, K. Kalantar-Zadeh, Nanostructured copper oxide semiconductors: a perspective on materials, synthesis methods and applications, Journal of Materials Chemistry C, 2 (2014) 5247-5270.
10. P. Poulopoulos, S. Baskoutas, S. D. Pappas, C. S. Garoufalis, S. A. Droulias, A. Zamani, V. Kapaklis, Intense quantum confinement effects in Cu_2O thin films, The Journal of Physical Chemistry C, 115 (2011) 14839-14843.
11. D. Ren, Y. Deng, A. D. Handoko, C. S. Chen, S. Malkhandi, B. S. Yeo, Selective electrochemical reduction of carbon dioxide to ethylene and ethanol on copper (I) oxide catalysts, Acs Catalysis, 5 (2015) 2814-2821.
12. K. H. V. Reddy, V. P. Reddy, J. Shankar, B. Madhav, B.S.P.A. Kumar, Y.V.D. Nageswar, Copper oxide nanoparticles catalyzed synthesis of aryl sulfides via cascade reaction of aryl halides with thiourea, Tetrahedron letters, 52 (2011) 2679-2682.
13. Y. Guo, M. Dai, Z. Zhu, Y. Chen, H. He, T. Qin, Chitosan modified Cu_2O nanoparticles with high catalytic activity for p-nitrophenol reduction, Applied Surface Science, 480 (2019) 601-610.
14. T. H. Mahato, B. Singh, A. K. Srivastava, G. K. Prasad, A. R. Srivastava, K. Ganesan, R. Vijayaraghavan, Effect of calcinations temperature of CuO nanoparticle on the kinetics of decontamination and decontamination products of sulphur mustard, Journal of hazardous materials, 192 (2011) 1890-1895.
15. Gajendiran, C. Ramamoorthy, K.C.P. Sankar, T.R.S. Kingsly, V. Kamalakannan, T. Krishnamoorthy, Optical and luminescent properties of NiO-CuO nanoparticle by the precipitation method, Journal of Advanced Chemical Sciences, (2016) 227-229.
16. Y. Li, B. Tan, Y. Wu, Mesoporous Co_3O_4 nanowire arrays for lithium ion batteries with high capacity and rate capability, Nano letters, 8 (2008) 265-270.
17. Y. Chen, Y. Zhang, S. Fu, Synthesis and characterization of Co_3O_4 hollow spheres, Materials Letters, 61 (2007) 701-705.
18. V. R. Shinde, S. B. Mahadik, T. P. Gujar, C. D. Lokhande, Supercapacitive cobalt oxide (Co_3O_4) thin films by spray pyrolysis, Applied Surface Science, 252 (2006) 7487-7492.
19. X. Liu, G. Qiu, X. Li, Shape-controlled synthesis and properties of uniform spinel cobalt oxide nanocubes, Nanotechnology, 16 (2005) 3035.
20. W.-W. Wang, Y.-J. Zhu, G.-F. Cheng, Y.-H. Huang, Microwave-assisted synthesis of cupric oxide nanosheets and nanowhiskers, Materials Letters, 60 (2006) 609-612.
21. E. Ding, A. Li, H. Liu, W. Liu, F. Chen, T. Li, B. Wang, Facile synthesis of ultrathin two-dimensional nanosheets-constructed MCo_2O_4 (M = Ni, Cu, Zn) nanotubes for efficient photocatalytic oxygen evolution, Nanoscale, 10 (2018) 3871-3876.

22. V. S. Kiran, S. Sumathi, Comparison of catalytic activity of bismuth substituted cobalt ferrite nanoparticles synthesized by combustion and co-precipitation method, Journal of Magnetism and Magnetic Materials, 421 (2017) 113-119.
23. H. Zhu, C. Zhang, Y. Yin, Novel synthesis of copper nanoparticles: influence of the synthesis conditions on the particle size, Nanotechnology, 16 (2005) 3079.
24. N. M. Deraz, A. Alarifi, Novel preparation and properties of magnesioferrite nanoparticles, Journal of analytical and applied pyrolysis, 97 (2012) 55-61.
25. N. M. Deraz, Fabrication, characterization and magnetic behaviour of alumina-doped zinc ferrite nano-particles, Journal of analytical and applied pyrolysis, 91 (2011) 48-54.
26. S.M.N. Jeghan, M. Kang, Facile synthesis and photocatalytic activity of cubic spinel urchin-like copper cobaltite architecture, Materials Research Bulletin, 91 (2017) 108-113.
27. Y.-q. Zhao, Y. Zhang, K.-z. Xu, Effect of Precursor on the Morphology and Supercapacitor Performance of $CuCo_2O_4$, Int. J. Electrochem. Sci, 14 (2019) 3885-3896.
28. R. Yuvasravana, P. P. George, N. Devanna, A Green-Chemical Approach for the Synthesis of Cobaltate Spinels MCo_2O_4 [M = Mg And Ni] Under Microwave Assistance, Inter. J. Innovative Res in Sci. Eng. Tech, 6 (2017) 11256.
29. S. M. Salem, Nasrallah M. Deraz, Hisham A. Saleh, Fabrication and characterization of chemically deposited copper–manganese sulfde thin flms, Applied Physics A, 127 (2020) 700.
30. A. K. Jonscher, Dielectric relaxation in solids, Chelsea, Dielectrics Pub., London, (1983).
31. M. L. Hassan, A. F. Ali, A. H. Salama, A. M. Abdel-Karim, Novel cellulose nanofibers/barium titanate nanoparticles nanoparticles and their electrical properties, Journal of Physical Organic Chemistry, 32 (2019) e3897.
32. A. M. Abdel-Karim, A. H. Salama, F. A. El-Samahy, M. El-Sedik, F. H. Osman, Some dielectric properties of novel nano-s-triazine derivatives, Journal of Physical Organic Chemistry, 30 (2017) e3703.
33. B. Chi, H. Lin, J. Li, Cations distribution of $Cu_xCo_3{-}xO_4$ and its electrocatalytic activities for oxygen evolution reaction, international journal of hydrogen energy, 33 (2008) 4763-4768.
34. A. Voronova, I. Ivanenko, Structural and catalytic properties of Ni-, Co-spinel, and its composites, Applied Nanoscience, (2020) 1-11.
35. M. R. Patil, M. K. Rendale, S. N. Mathad, R. B. Pujar, Structural and IR study of Ni 0.5–xCdx$Zn_{0.5}Fe_2O_4$, International Journal of Self-Propagating High-Temperature Synthesis, 24 (2015) 241-245.
36. S. N. Mathad, R. N. Jadhav, N. D. Patil, V. Puri, Structural and mechanical properties of Sr^+ 2-doped bismuth manganite thick films, International Journal of Self-Propagating High-Temperature Synthesis, 22 (2013) 180-184.
37. S. N. Mathad, R. N. Jadhav, V. Phadtare, V. Puri, Structural and mechanical properties of Sr-doped barium niobate thick films, International Journal of Self-Propagating High-Temperature Synthesis, 23 (2014) 145-150.
38. C. Rath, S. Anand, R. P. Das, K. K. Sahu, S. D. Kulkarni, S. K. Date, N. C. Mishra, Dependence on cation distribution of particle size, lattice parameter, and magnetic properties in nanosize Mn–Zn ferrite, Journal of Applied Physics, 91 (2002) 2211-2215.
39. N.-A. M. Deraz, The formation and physicochemical characterization of Al_2O_3-doped manganese ferrites, Thermochimica acta, 401 (2003) 175-185.

40. Z.-Y. Tian, N. Bahlawane, V. Vannier, K. Kohse-Höinghaus, Structure sensitivity of propene oxidation over Co-Mn spinels, Proceedings of the Combustion Institute, 34 (2013) 2261-2268.
41. Y. Li, W. Liu, M. Wu, Z. Yi, J. Zhang, Oxidation of 2, 3, 5-trimethylphenol to 2, 3, 5-trimethylbenzoquinone with aqueous hydrogen peroxide in the presence of spinel $CuCo_2O_4$, Journal of Molecular Catalysis A: Chemical, 261 (2007) 73-78.
42. K. Nakamoto, Infrared and Raman Spectra of Inorganic and Coordination Compounds, by John Willey and Sons, Inc, New York, (1986).
43. A. J. Reddy, M. K. Kokila, H. Nagabhushana, R.P.S. Chakradhar, C. Shivakumara, J. L. Rao, B. M. Nagabhushana, Structural, optical and EPR studies on ZnO: Cu nanopowders prepared via low temperature solution combustion synthesis, Journal of Alloys and Compounds, 509 (2011) 5349-5355.
44. J. T. Kloprogge, L. Hickey, R. L. Frost, FT-Raman and FT-IR spectroscopic study of synthetic Mg/Zn/Al-hydrotalcites, Journal of Raman Spectroscopy, 35 (2004) 967-974.
45. E. M. Mohammed, K. A. Malini, P. Kurian, M. R. Anantharaman, Modification of dielectric and mechanical properties of rubber ferrite composites containing manganese zinc ferrite, Materials research bulletin, 37 (2002) 753-768.
46. R. D. Waldron, Infrared spectra of ferrites, Physical review, 99 (1955) 1727.
47. I. Ivanenko, A. Voronova, I. Astrelin, Y. Romanenko, Structural and catalytic properties of Ni–Co spinel and its composites, Bulletin of Materials Science, 42 (2019) 172.
48. N. Kattan, B. Hou, D. J. Fermín, D. Cherns, Crystal structure and defects visualization of Cu_2ZnSnS_4 nanoparticles employing transmission electron microscopy and electron diffraction, Applied Materials Today, 1 (2015) 52-59.
49. J. Zheng, X. Liu, L. Zhang, Design of porous double-shell Cu_2O@ $CuCo_2O_4$ Z-Scheme hollow microspheres with superior redox property for synergistic photocatalytic degradation of multi-pollutants, Chemical Engineering Journal, 389 (2020) 124339.
50. S. Saha, M. Jana, P. Khanra, P. Samanta, H. Koo, N. C. Murmu, T. Kuila, Band gap modified boron doped NiO/Fe_3O_4 nanostructure as the positive electrode for high energy asymmetric supercapacitors, RSC advances, 6 (2016) 1380-1387.
51. Z.-Y. Tian, H. Vieker, P. M. Kouotou, A. Beyer, In situ characterization of Cu–Co oxides for catalytic application, Faraday discussions, 177 (2015) 249-262.
52. E.J.W. Verwey, J.H. De Boer, Cation arrangement in a few oxides with crystal structures of the spinel type, Recueil des Travaux Chimiques des Pays-Bas, 55 (1936) 531-540.
53. M.S.R. Prasad, B. Prasad, B. Rajesh, K.H. Rao, K.V. Ramesh, Magnetic properties and DC electrical resistivity studies on cadmium substituted nickel–zinc ferrite system, Journal of magnetism and magnetic materials, 323 (2011) 2115-2121.
54. A. K. Jonscher, Universal relaxation law: a sequel to Dielectric relaxation in solids, Chelsea Dielectrics Press, 1996.
55. E. Barsoukov, MacDonald, JR (Hrsg.): Impedance Spectroscopy. Hoboken, in, New Jersey: Wiley-Interscience, 2005.
56. M. Vijayakumar, S. Selvasekarapandian, M. S. Bhuvaneswari, G. Hirankumar, G. Ramprasad, R. Subramanian, P. C. Angelo, Synthesis and ion dynamics studies of nanocrystalline Mg stabilized zirconia, Physica B: Condensed Matter, 334 (2003) 390-397.
57. S. R. Elliott, Frequency-dependent conductivity in ionically and electronically conducting amorphous solids, Solid State Ionics, 70 (1994) 27-40.
58. M. A. Afifi, A. E. Bekheet, E. A. Elwahhab, H. E. Atyia, Ac conductivity and dielectric properties of amorphous In_2Se_3 films, Vacuum, 61 (2001) 9-17.

59. K.S. Rao, D.M. Prasad, P.M. Krishna, B. Tilak, K.C. Varadarajulu, Impedance and modulus spectroscopy studies on $Ba_{0.1}Sr_{0.81}La_{0.06}Bi_2Nb_2O_9$ ceramic, Materials Science and Engineering: B, 133 (2006) 141-150.
60. L.L. Hench, J.K. West, Principles of electronic ceramics, (1989).
61. A.K. Singh, T.C. Goel, R.G. Mendiratta, O.P. Thakur, C. Prakash, Dielectric properties of Mn-substituted Ni–Zn ferrites, Journal of applied physics, 91 (2002) 6626-6629.
62. H.S.C. O'Neill, A. Navrotsky, Simple spinels; crystallographic parameters, cation radii, lattice energies, and cation distribution, American Mineralogist, 68 (1983) 181-194.
63. R.S. Devan, Y.D. Kolekar, B.K. Chougule, Effect of cobalt substitution on the properties of nickel–copper ferrite, Journal of Physics: Condensed Matter, 18 (2006) 9809.
64. S.S. Kumbhar, M.A. Mahadik, V.S. Mohite, K.Y. Rajpure, J.H. Kim, A.V. Moholkar, C.H. Bhosale, Structural, dielectric and magnetic properties of Ni substituted zinc ferrite, Journal of magnetism and magnetic materials, 363 (2014) 114-120.
65. A. S. Fawzi, A. D. Sheikh, V. L. Mathe, Structural, dielectric properties and AC conductivity of $Ni_{(1-x)}Zn_xFe_2O_4$ spinel ferrites, Journal of Alloys and Compounds, 502 (2010) 231-237.
66. R.G. Kharabe, R.S. Devan, C.M. Kanamadi, B.K. Chougule, Dielectric properties of mixed Li–Ni–Cd ferrites, Smart Materials and Structures, 15 (2006) N36.
67. Filipović Suzana, et al.,"Structure and properties of nanocrystalline tetragonal $BaTiO_3$ prepared by combustion solid state synthesis", Science of Sintering, 52 (3) (2020) 257-268.
68. Maitreekeaw Kanchana, Tawat Chanadee,"Calcium Titanate Ceramics Obtained by Combustion Synthesis and Two-Step Sintering", Science of Sintering, 52(4) (2020) 491-502.

Сажетак: *Серија композита $CuO/CuCo_2O_4$ је припремљена методом сагоревања на 750 ^oC са различитим моларним односом Cu/Co. Карактеризација различитих композита је систематски испитана разним аналитичким техникама. Рендгенска дифракција и FTIR указују на раст добро искристалисаних наночестица $CuCo_2O_4$ кубне спинелне структуре. Слике TEM и CEM микроскопије указују на равномерну расподелу честица. Из UV-видљивог спектра, израчунате ширине забрањених зона су биле у рангу од 1.2 и 1.8eV за различите саставе. Електрична својства су мерена на температурама између 303 и 463K у фреквентном опсегу 102-106Hz. AC проводљивост задовољава Jonscher једначину, посебно на високим фреквенцијама. Добијени резултати мерене проводљивости и диелектричне константе указују да се припремљени узорци понашају као полупроводни материјали. Коначно, можемо да закључимо да композити $CuO/CuCo_2O_4$ показују атрактивна мулти-функционална својства за електричну примену.*

Кључне речи*: $CuO/CuCo_2O_4$ композит; оптичка својства, проводљивост, диелектрична константа, полупроводници.*